JACS
JOURNAL OF THE AMERICAN CHEMICAL SOCIETY
Article
pubs.acs.org/JACS

Stabilizing Cesium Lead Halide Perovskite Lattice through Mn(II) Substitution for Air-Stable Light-Emitting Diodes

Shenghan Zou,[†,‡,§,#] Yongsheng Liu,[*,†] Jianhai Li,[⊥] Caiping Liu,[†] Rui Feng,[¶] Feilong Jiang,[†] Yongxiang Li,[#] Jizhong Song,[⊥] Haibo Zeng,[*,⊥] Maochun Hong,[*,†] and Xueyuan Chen[*,†]

[†]CAS Key Laboratory of Design and Assembly of Functional Nanostructures, CAS Key Laboratory of Optoelectronic Materials Chemistry and Physics, and State Key Laboratory of Structural Chemistry, Fujian Institute of Research on the Structure of Matter, Chinese Academy of Sciences, Fuzhou, Fujian 350002, China

[⊥]MIIT Key Laboratory of Advanced Display Materials and Devices, Institute of Optoelectronics and Nanomaterials, School of Materials Science and Engineering, Nanjing University of Science and Technology, Nanjing 210094, China

[¶]Testing Center, Fuzhou University, Fuzhou, Fujian 350002, China

[‡]University of the Chinese Academy of Sciences, Beijing 100049, China

[§]School of Physical Science and Technology, ShanghaiTech University, Shanghai 201210, China

[#]Shanghai Institute of Ceramics, Chinese Academy of Sciences, Shanghai 200050, China

Supporting Information

ABSTRACT: All-inorganic cesium lead halide perovskite ($CsPbX_3$, X = Cl, Br, and I) quantum dots (QDs), possessing high photoluminescence quantum yields and tunable color output, have recently been endowed great promise for high-performance solar cells and light-emitting diodes (LEDs). Although moisture stability has been greatly improved through separating QDs with a SiO_2 shell, the practical applications of $CsPbX_3$ QDs are severely restricted by their poor thermal stability, which is associated with the intrinsically low formation energies of perovskite lattices. In this regard, enhancing the formation energies of perovskite lattices of $CsPbX_3$ QDs holds great promise in getting to the root of their poor thermal stability, which hitherto remains untouched. Herein, we demonstrate an effective strategy through Mn^{2+} substitution to fundamentally stabilize perovskite lattices of $CsPbX_3$ QDs even at high temperatures up to 200 °C under ambient air conditions. We employ first-principle calculations to confirm that the significantly improved thermal stability and optical performance of $CsPbX_3$:Mn^{2+} QDs arise primarily from the enhanced formation energy due to the successful doping of Mn^{2+} in $CsPbX_3$ QDs. Benefiting from such an effective substitution strategy, these Mn^{2+}-doped $CsPbX_3$ QDs can function well as efficient light emitters toward the fabrication of high-performance perovskite LEDs.

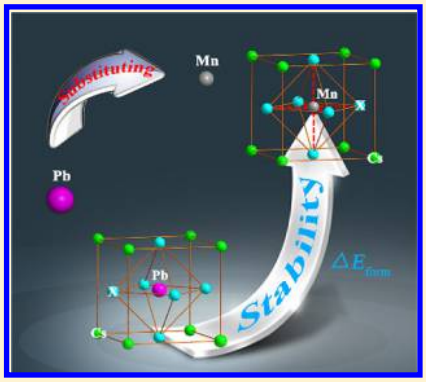

INTRODUCTION

The past several years have witnessed the rapid development of all-inorganic cesium lead halide perovskite ($CsPbX_3$, X = Cl, Br, and I) quantum dots (QDs).[1−16] Their exceptional optical properties, including tunable photoluminescence (PL) outputs, high PL quantum yields (QYs), and narrow emission line widths, make them particularly suitable as promising candidate materials for optoelectronic applications in areas as diverse as solar cells, lasing, and light-emitting diodes (LEDs).[17−31] Although moisture stability of $CsPbX_3$ QDs has been greatly improved through some approaches such as surface chloride doping,[18] low-flux X-ray irradiation,[32] and coating the QDs with inert mesoporous silica,[33−35] their practical applications are severely restricted by the poor thermal stability of perovskite $CsPbX_3$ QDs.[20,33,37−40] In principle, such notorious thermal instability of $CsPbX_3$ QDs originates primarily from their low formation energies of perovskite lattices analogous to hybrid organic−inorganic halide perovskites.[35,36] In this regard, enhancing the formation energies of perovskite lattices of $CsPbX_3$ QDs holds great promise in getting to the root of their poor thermal stability, which hitherto remains untouched.

For nanomaterials, impurity doping that incorporates different ions of appropriate elements into host lattices has been extensively explored as an effective approach to stabilize specific crystallographic phases and to modulate the optical and electronic performance of diverse nanocrystals.[37−41] Particularly, the Son, Sheldon, and Zhang groups have recently demonstrated that Mn^{2+} ions can be introduced into the lattices of perovskite $CsPbX_3$ QDs by using a well-designed synthetic approach.[38,42,43] Motivated by their identical octahedral coordination environment of host cations formed by six halide atoms for $CsPbX_3$ and $CsMnX_3$ crystals (Figure 1a) coupled with the higher formation energies of $CsMnX_3$ relative to those of $CsPbX_3$ crystals (Tables S1), we speculate that the doping of trace amounts of Mn^{2+} (~0.97 Å), with an ionic radius smaller

Received: April 20, 2017
Published: July 31, 2017

DOI: 10.1021/jacs.7b04000
J. Am. Chem. Soc. 2017, 139, 11443−11450

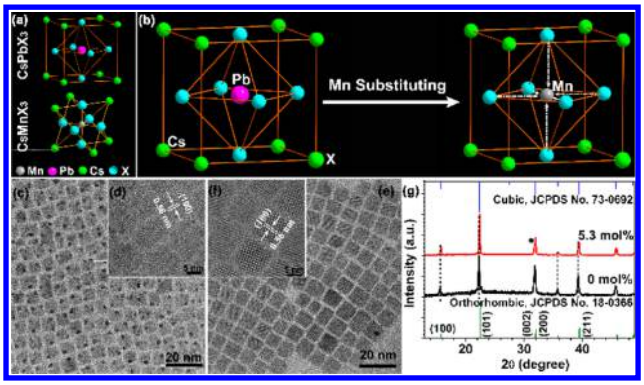

Figure 1. (a) Schematic illustration showing the crystal structures of perovskite $CsPbX_3$ and $CsNiCl_3$-structured $CsMnX_3$ with identical octahedral coordination environment of host cation formed by six halide atoms. (b) Schematic illustration showing the lattice contraction in a perovskite $CsPbX_3$ crystal after the substitution of Pb^{2+} with smaller Mn^{2+} ions. TEM and high-resolution TEM images for (c, d) pure and (e, f) $CsPbCl_3$:Mn QDs and their corresponding (g) XRD patterns showing that all XRD peaks can be indexed in accordance with an orthorhombic perovskite $CsPbCl_3$ crystal structure (JCPDS No. 18-0366).

than Pb^{2+} (~1.33 Å),[38] in perovskite $CsPbX_3$ lattices can enhance the formation energies of perovskite $CsPbX_3$ QDs and thus fundamentally circumvent their poor thermal stability (Figure 1b). Herein, we demonstrate for the first time that the perovskite lattices of $CsPbX_3$ QDs can be fundamentally stabilized under ambient air conditions through such a Mn^{2+}-substitution strategy. We adopt first-principle calculations to confirm that the much improved thermal stability and optical performance for perovskite $CsPbX_3$ QDs arises mainly from the enhanced formation energies due to the successful doping of Mn^{2+} ions in perovskite lattices of $CsPbX_3$ QDs. Benefiting from such greatly improved thermal stability and optical performance, these Mn^{2+}-doped $CsPbX_3$ QDs can function very well as efficient light emitters to fabricate high-performance perovskite LEDs (PLEDs) with higher maximum luminance, external quantum efficiency (EQE), and current efficiency (CE) when compared to the PLEDs based on pure $CsPbX_3$ QDs.

■ RESULTS AND DISCUSSION

Monodisperse $CsPbX_3$ QDs doped with Mn^{2+} ions at nominal concentrations ranging from 0 to 60 mol % (hereafter referred to as $CsPbX_3$:Mn) were synthesized according to a previously reported method with some modifications.[2] The actual Mn^{2+} doping concentrations in $CsPbX_3$ QDs determined from inductively coupled plasma atomic emission spectroscopy (ICP-AES) were observed to deviate considerably from their nominal ones as previously observed in Mn^{2+}-doped $CsPbCl_3$ QDs (Table S2).[42] Representative transmission electron microscopy (TEM) images show that the as-synthesized $CsPbCl_3$:Mn QDs have a nearly cubic morphology with an average size of 8.6 ± 0.5 nm, which is slightly larger than their pure counterparts (7.9 ± 0.5 nm) (Figures 1c−f and S1). Clear lattice fringes were also observed for orthorhombic perovskite $CsPbX_3$:Mn QDs, indicating that the crystallinity for $CsPbX_3$:Mn QDs is comparable to their pure counterparts (Figures 1d,f and S2). This result was further confirmed by the slightly reduced full-width at half-maximum (fwhm) of powder X-ray diffraction (XRD) peaks with increased Mn^{2+} doping concentration, where all the XRD peaks for $CsPbCl_3$:Mn and $CsPbBr_3$:Mn QDs can be well indexed as orthorhombic perovskite $CsPbX_3$ structures (Figures 1g and S3).[7] Importantly, we also observed that the XRD peaks shift toward higher diffraction angles in the XRD patterns as a result of the lattice contraction owing to the substitution of Pb^{2+} ions by smaller Mn^{2+} ions in host lattices (Figures 1g and S3).[38,43]

In order to probe the local structure around Mn^{2+} ions in $CsPbX_3$ QDs, we first investigated the PL properties of pure and Mn-doped $CsPbX_3$ QDs at room temperature (Figures 2 and S4). For instance, upon UV excitation of $CsPbCl_3$ QDs at 362 nm, which corresponds to their band gap absorption, a pure $CsPbCl_3$ sample exhibits characteristic excitonic luminescence centered at ~404 nm, while the PL emission spectrum of $CsPbCl_3$:Mn (5.8 mol %) QDs features a dominant broad emission band peaking at ~600 nm along with the secondary excitonic luminescence of the perovskite host, which can be readily ascribed to the $^4T_1 \rightarrow {}^6A_1$ transition of Mn^{2+} doped in $CsPbCl_3$ QDs (Figure 2a).[42,44,45] The PL lifetime of Mn^{2+} was determined to be ~1.2 ms, which is distinct from the short-lived excitonic luminescence (with a lifetime of 3.2−5 ns, Figure S5). The intensity for broad-band emission of Mn^{2+} ion was observed to enhance gradually with increased nominal

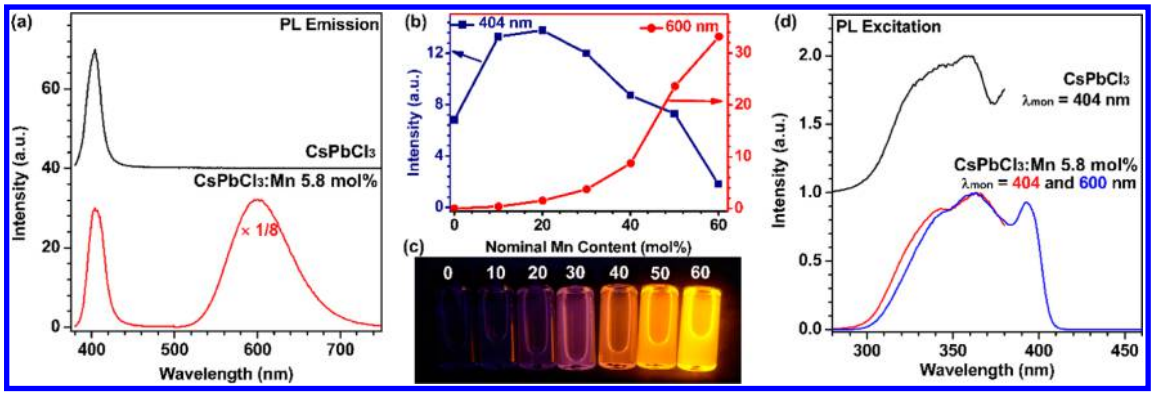

Figure 2. (a) Comparison of typical PL emission spectra for pure $CsPbCl_3$ and $CsPbCl_3$:Mn (5.8 mol %) QDs upon UV excitation at 362 nm. (b) PL intensities for excitonic or Mn^{2+}-related emissions of $CsPbCl_3$:Mn QDs centered at 404 and 600 nm as a function of the nominal doping concentration of Mn^{2+} ions ranging from 0 to 60 mol % and their corresponding (c) PL emission photographs in cyclohexane solution under 362 nm UV lamp irradiation. Note that the nominal Mn^{2+} doping concentration was used herein for clarity. (d) Comparison of PL excitation spectra for pure $CsPbCl_3$ and $CsPbCl_3$:Mn (5.8 mol %) QDs by monitoring the excitonic or Mn^{2+}-related emissions centered at 404 and 600 nm, respectively.

DOI: 10.1021/jacs.7b04000
J. Am. Chem. Soc. 2017, 139, 11443−11450

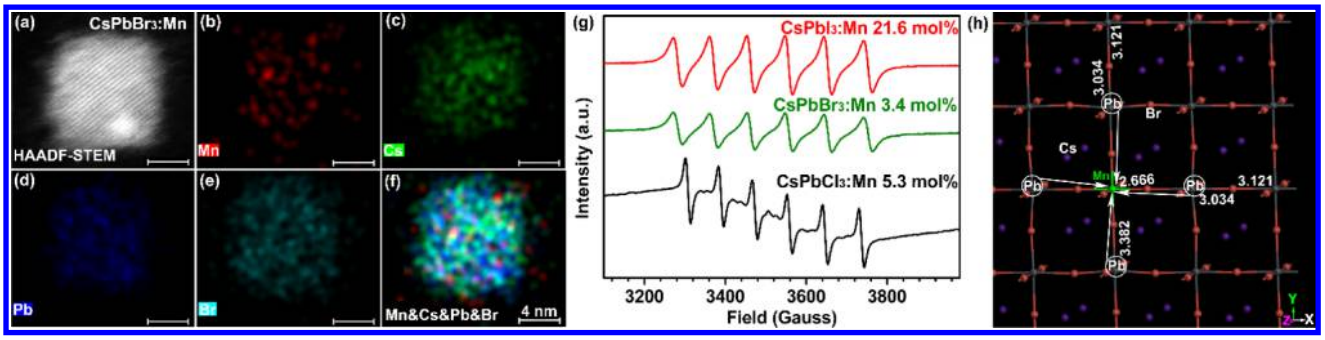

Figure 3. (a) HAADF-STEM image of a single randomly selected $CsPbBr_3$:Mn (3.4 mol %) QD and (b−f) its corresponding EDS element mapping images of Mn, Cs, Pb, and Br. (g) X-band EPR spectra for $CsPbX_3$:Mn QDs measured at room temperature, demonstrating the successful substitution of Pb^{2+} with Mn^{2+} in the lattices of $CsPbX_3$ QDs. (h) Calculated three-dimensional stacking diagram of a $CsPbBr_3$:Mn crystal when Pb^{2+} ion was substituted by Mn^{2+} ion with an actual concentration of 2.08 mol % by using first-principle calculations based on DFT, showing the lattice contraction in the (001) lattice plane of an orthorhombic perovskite $CsPbBr_3$ crystal induced by Mn^{2+} doping.

Mn^{2+} doping concentration, which differs markedly from the excitonic PL behavior of $CsPbCl_3$:Mn QDs that show a declining trend after an initial rise in PL intensity (Figure 2b). Such an emission tuning gave rise to overall color outputs from blue to orange-red that are visible to the naked eye (Figure 2c). Accordingly, the absolute PL QY was observed to increase remarkably from 0.6% for pure $CsPbCl_3$ QDs to 12.7% for $CsPbCl_3$:Mn^{2+} QDs with a nominal Mn^{2+} doping concentration of 60 mol % upon 362 nm UV lamp excitation (Figure S6). Notably, it was found that both pure $CsPbCl_3$ and $CsPbCl_3$:Mn QDs exhibit almost the same PL excitation spectra by monitoring their excitonic or Mn^{2+}-related emissions centered at 404 and 600 nm (Figure 2d), respectively, suggesting that the broad-band emission of Mn^{2+} occurs from an efficient $CsPbCl_3$ host to Mn^{2+} energy transfer. In this process, the $CsPbCl_3$ host acts as an efficient light-harvesting antenna to absorb UV excitation light and subsequently transfer its energy to the doped Mn^{2+} ions, resulting in the overall red emission of Mn^{2+}, as shown in the PL photographs in Figure 2c. Note that such broad-band emission of Mn^{2+} can hardly be detected in either $CsMnCl_3$ or $CsPbCl_3$ QDs with Mn^{2+} emitters adsorbed on their surfaces (not shown). These results vindicate unambiguously that the Mn^{2+} ions were preferentially incorporated into the lattices of $CsPbX_3$ QDs rather than on their surface, as indicated by the observation of gradually decreased PL lifetime with the increased Mn^{2+} content when monitoring the excitonic luminescence of $CsPbX_3$:Mn^{2+} QDs (Figures S5 and S7).

Although such a $CsPbX_3$ host to Mn^{2+} energy transfer cannot be detected in $CsPbBr_3$:Mn^{2+} and $CsPbI_3$:Mn^{2+} QDs due to the mismatch between their band gap absorption and $^4T_1 \rightarrow {}^6A_1$ transition of Mn^{2+},[38,46] the Mn^{2+} ion was found to have a significant impact on their PL behaviors. Both the PL intensity (Figure S4) and QY (Figure S8) for excitonic luminescence of $CsPbBr_3$:Mn^{2+} and $CsPbI_3$:Mn^{2+} QDs were detected to increase first and then decrease when doping with increased Mn^{2+} concentrations, thereby providing more solid evidence to verify the successful doping of Mn^{2+} ions in $CsPbX_3$ QDs. To determine the actual location of Mn^{2+} ions in $CsPbX_3$ QDs, we performed energy dispersive X-ray spectroscopy (EDS) element mapping and obtained room-temperature X-band electron paramagnetic resonance (EPR) spectra of $CsPbX_3$:Mn QDs. The high-angle annular dark-field scanning transmission electron microscopy (HAADF-STEM) image (Figure 3a) coupled with the corresponding EDS element mapping of some randomly selected $CsPbX_3$:Mn^{2+} QDs (Figures 3b−f and S9) show that Mn^{2+} ions are homogeneously distributed among all the QDs, indicative of the successful doping of Mn^{2+} in $CsPbX_3$:Mn^{2+} QDs. More importantly, all the $CsPbX_3$:Mn QDs were observed to exhibit sharp sextet hyperfine splitting of X-band EPR patterns of Mn^{2+} ions analogous to that detected in Mn^{2+}-doped $CsPbCl_3$ bulk materials with Mn^{2+} ions occupying a substituted Pb^{2+} site (Figure 3g),[42,46] which clearly demonstrates that the Mn^{2+} ions experience a substitutional Pb^{2+} octahedral coordination environment in the lattices of $CsPbX_3$ QDs particularly for $CsPbBr_3$ and $CsPbI_3$.

To shed more light on the doping of Mn^{2+} in the lattices of $CsPbX_3$ QDs, we then carried out first-principle calculations based on density functional theory (DFT) for the formation energy (ΔE_{form}, defined as the change in energy when a nanocrystal is formed from its isolated atoms) and some bond lengths of $CsMnBr_3$, $CsPbBr_3$, and $CsPbBr_3$:Mn QDs (Tables 1 and S3), provided that Mn^{2+} ions reside in the substitutional Pb^{2+} lattice site in the perovskite $CsPbBr_3$ crystal. As compared in Table 1, the absolute value of ΔE_{form} per Pb^{2+} (or Mn^{2+}) ion was observed to rise slightly with increased Mn^{2+} content, reaching a maximum at ∼2.08 mol %, and then decreased rapidly with further increasing the doping content of Mn^{2+} in $CsPbBr_3$ QDs. For instance, the absolute value of ΔE_{form} per Pb^{2+} (or Mn^{2+}) ion for $CsPbBr_3$:Mn QDs (−6.77 eV) was determined to increase by about 0.32 eV when Pb^{2+} is replaced by Mn^{2+} with a content of 2.08 mol % (−6.45 eV for pure

Table 1. Calculated Formation Energies for Perovskite $CsPbBr_3$ QDs Doped with Different Mn^{2+} and Sn^{2+} Contents by Using First-Principle Calculations Based on DFT

crystal	dopant content (mol %)	ΔE_{form} (per divalent ion, eV)
$CsPbBr_3$	0	−6.45
$Cs_{64}Mn_1Pb_{63}Br_{192}$	1.56	−6.47
$Cs_{48}Mn_1Pb_{47}Br_{144}$	2.08	−6.77
$Cs_{32}Mn_1Pb_{31}Br_{96}$	3.13	−6.75
$Cs_{27}Mn_1Pb_{26}Br_{81}$	3.70	−6.72
$Cs_{18}Mn_1Pb_{17}Br_{54}$	5.67	−6.39
$Cs_{16}Mn_1Pb_{15}Br_{48}$	6.25	−6.37
$Cs_{12}Mn_1Pb_{11}Br_{36}$	8.33	−6.27
$Cs_{10}Mn_1Pb_9Br_{30}$	10.0	−6.20
$Cs_8Mn_1Pb_7Br_{24}$	12.5	−6.10
$Cs_4Mn_1Pb_3Br_{12}$	25.0	−5.21
$CsMnBr_3$	100	−15.54
$Cs_{48}Sn_1Pb_{47}Br_{144}$	2.08	−6.85

DOI: 10.1021/jacs.7b04000
J. Am. Chem. Soc. 2017, 139, 11443−11450

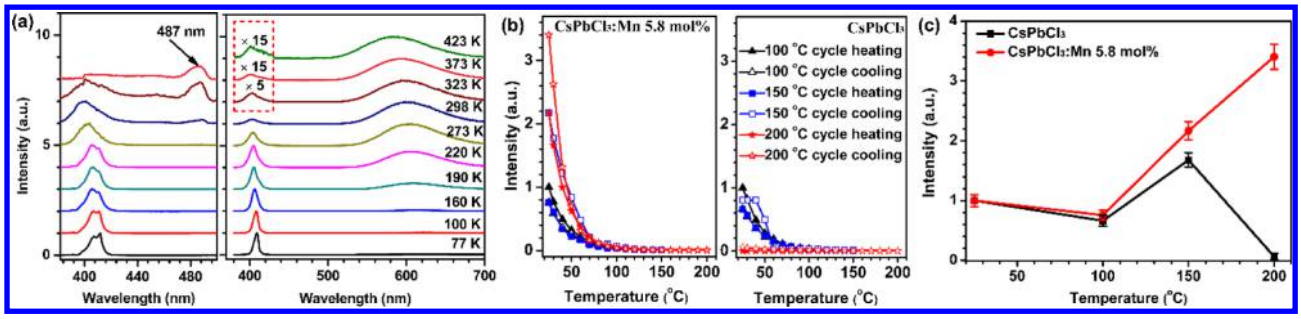

Figure 4. (a) Temperature evolution for PL emission spectra of pure $CsPbCl_3$ and $CsPbCl_3$:Mn (5.8 mol %) QDs upon UV excitation at 362 nm. (b) Temperature-dependent PL intensities for excitonic luminescence of $CsPbCl_3$:Mn (5.8 mol %) and pure $CsPbCl_3$ QDs via three heating/cooling cycles at 100, 150, and 200 °C, respectively, and (c) the room-temperature integrated PL intensities of $CsPbCl_3$:Mn and pure $CsPbCl_3$ QDs after the above three heating/cooling cycles.

$CsPbBr_3$), which corroborates that $CsPbX_3$:Mn QDs are more energetically stable than their counterparts without Mn^{2+} doping. In other words, replacing Pb^{2+} with Mn^{2+} in the lattices of $CsPbX_3$ QDs is thermodynamically favored regardless of their large discrepancy in ionic radius. In this sense, the optimal doping concentration of Mn^{2+} (or Mn^{2+}/Pb^{2+} mole ratio) is theoretically predicted to be ∼2.08 mol % to yield the most thermodynamically stable QDs. Our calculations are well consistent with our experimental observations showing that the $CsPbBr_3$:Mn QDs with a Mn^{2+} doping content of 2.6 mol % are much more stable than pure $CsPbBr_3$ or $CsPbBr_3$:Mn (4.3 mol %) counterparts, because the latter exhibited much more rapid degradation in both PL brightness and solution color when exposed to ambient air conditions (Figure S10).

In view of their large discrepancy in ionic radius, the substitution of Pb^{2+} with smaller Mn^{2+} in the lattices of $CsPbX_3$ QDs possessing an octahedral coordination environment might induce lattice contraction in perovskite $CsPbX_3$ QDs, as exemplified by the simulated three-dimensional stacking diagrams of $CsPbBr_3$:Mn QDs (2.08 mol %), where the bond length of Mn−Br (2.666 Å) was calculated to be much shorter than those of the first (3.382 Å) and second (3.034 Å) nearest-neighboring or normal (3.003 Å) Pb−Br bonds (Figure 3h and Table S3). Consistently, some lattice distortions can be occasionally detected in high-resolution TEM images for some randomly selected $CsPbBr_3$:Mn QDs, in stark contrast to the perfect lattice fringes of pure $CsPbBr_3$ QDs (Figure S11). Such lattice contractions may substantially stabilize $CsPbX_3$:Mn QDs and thus result in high-quality Mn^{2+}-doped perovskite QDs with much better thermal stability than their pure counterparts, as discussed in the following.

To evaluate the thermal stability of $CsPbX_3$:Mn QDs induced by Mn^{2+} doping, we compared the temperature-dependent PL emission spectra for pure $CsPbX_3$ and $CsPbX_3$:Mn (5.8 mol %) QDs in the temperature range of 77 to 473 K. As shown in Figure 4a, the PL spectra for pure $CsPbCl_3$ QDs exhibit an abnormal emission band centered at 487 nm when measured above 298 K, due likely to the formation of some other impurities such as Cs_2PbCl_6. By contrast, such an abnormal emission band cannot be detected at 487 nm even when heated to 423 K for $CsPbCl_3$:Mn QDs, indicating their much better thermal stability than pure $CsPbX_3$ counterparts. The excellent thermal stability of $CsPbX_3$:Mn QDs was further verified by gradually heating them to high temperatures (100, 150, and 200 °C) and then cooling to room temperature while monitoring their PL spectra at temperature intervals of 10 °C (Figure 4b). Notably, the room-temperature integrated PL intensity for excitonic luminescence of $CsPbCl_3$:Mn (5.8 mol %) QDs was found to be markedly enhanced by a factor of ∼3.4 relative to their initial PL intensity after being heated to 200 °C and then cooled to room temperature, which is totally different from the case of pure $CsPbCl_3$ QDs, whose PL emission was barely detectable after undergoing the same heating and cooling cycles (Figure 4b,c). Similarly, enhanced excitonic luminescence was also realized in Mn^{2+}-doped $CsPbBr_3$ (Figure 5a) and $CsPbI_3$ QDs (Figure S12). The room-temperature PL intensities for excitonic luminescence of $CsPbBr_3$:Mn (4.3 mol %) and $CsPbI_3$:Mn (7.9 mol %) can retain about 120% and 20% of their original initial intensities undergoing three heating and cooling cycles at 100, 150, and 200 °C, much better than those of their pure

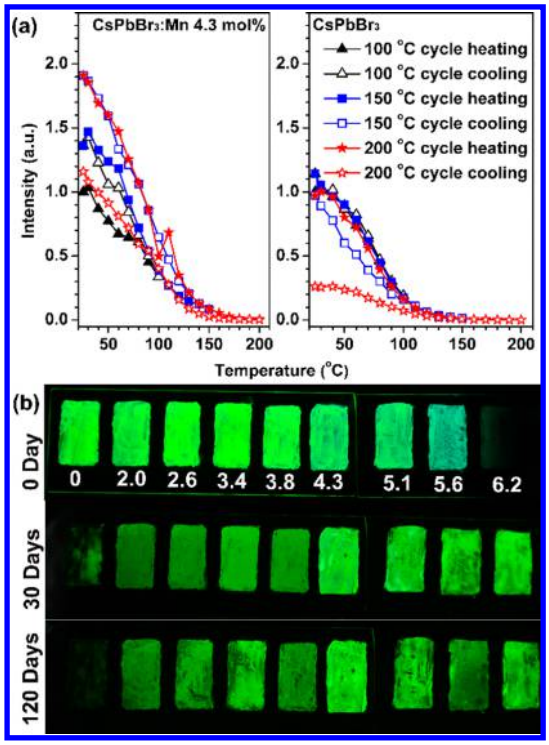

Figure 5. (a) Temperature-dependent PL intensities for excitonic luminescence of $CsPbBr_3$:Mn (4.3 mol %) and pure $CsPbBr_3$ QDs via three heating/cooling cycles at 100, 150, and 200 °C, respectively. (b) PL emission photographs for $CsPbBr_3$:Mn QDs coated on the surface of a glass slide with different Mn^{2+} contents from 0 to 6.2 mol % taken under UV irradiation at indicated time periods.

DOI: 10.1021/jacs.7b04000
J. Am. Chem. Soc. 2017, 139, 11443−11450

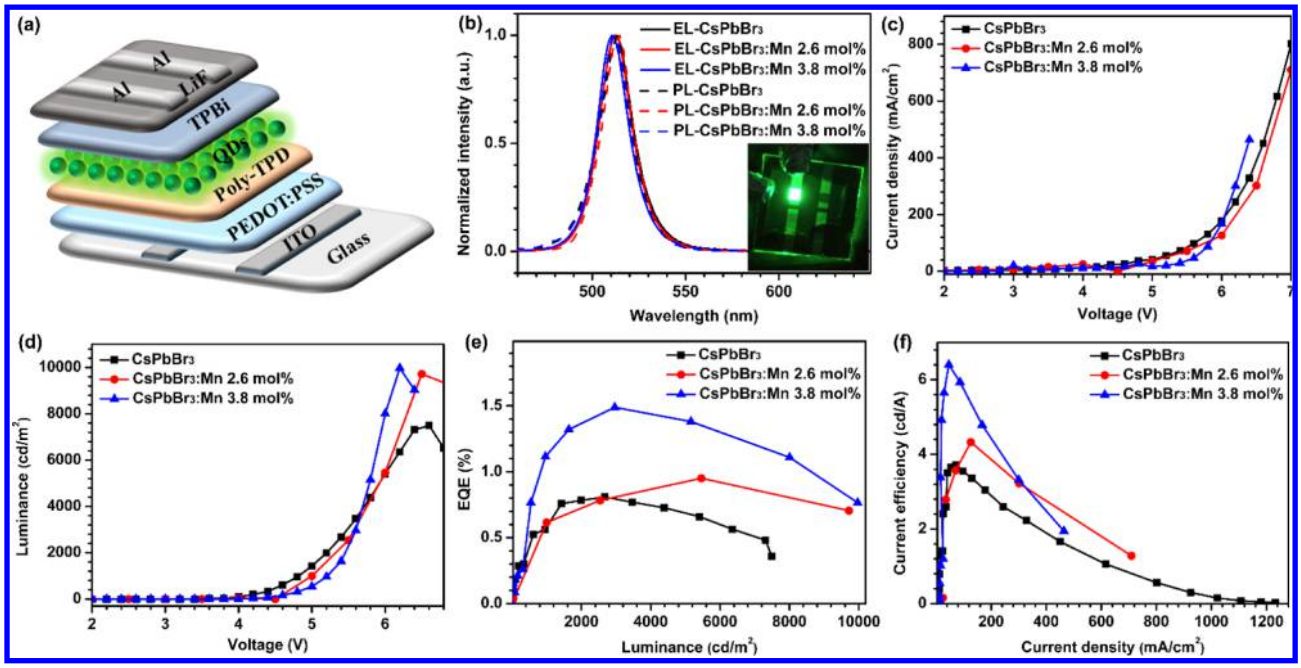

Figure 6. (a) Schematic illustration of a typical multilayer-structured PLED device by using pure $CsPbBr_3$ and $CsPbBr_3$:Mn (2.6 mol %) and $CsPbBr_3$:Mn (3.8 mol %) QDs as green light emitters. (b) Comparison of normalized EL spectra at an applied voltage of 6 V and their corresponding PL emission spectra for $CsPbBr_3$ and $CsPbBr_3$:Mn (2.6 mol %) and $CsPbBr_3$:Mn (3.8 mol %) QDs when dispersed in cyclohexane solution. The inset shows a photograph of the EL of a representative PLED device. Current density (c) and luminance (d) versus driving voltage characteristics for three types of PLEDs based on the pure $CsPbBr_3$ and $CsPbBr_3$:Mn (2.6 mol %), and $CsPbBr_3$:Mn (3.8 mol %) QDs. (e) EQE of these devices as a function of luminance. (f) Current efficiency of these devices as a function of current density.

counterparts, thereby demonstrating the critical role of Mn^{2+} doping in improving the thermal stability of the $CsPbX_3$ family. Such enhanced excitonic luminescence in Mn^{2+}-doped $CsPbX_3$ QDs is conceivable due to the fact that the excess Mn^{2+} dopants beyond their optimal doping concentration can be gradually excluded from the lattices of $CsPbX_3$ QDs when heated at high temperature, producing the most thermodynamically stable QDs with an optimal Mn^{2+} doping concentration of ~2.08 mol % and thus enhanced excitonic luminescence. This explanation is strongly supported by the gradually decreased Mn^{2+} emission observed in $CsPbCl_3$:Mn QDs after three heating/cooling cycles at 100, 150, and 200 °C, respectively (Figure S13).

Besides Mn^{2+} ions, we have extended our doping strategy in $CsPbBr_3$ QDs to Sn^{2+}, Cd^{2+}, Co^{2+}, Zn^{2+}, and Sr^{2+} ions, which possess smaller ionic radii than Pb^{2+}, and then performed first-principle calculations based on DFT to determine their formation energies. Among these divalent ions, the doping of Sn^{2+} ions in $CsPbBr_3$ QDs is expected to be easier than other divalent ions, because both the $CsSnBr_3$ and $CsPbBr_3$ crystals adopt identical ABX_3-type perovskite crystalline structures.[47−49] As a result, the actual doping concentration of Sn^{2+} was determined to be much higher than other divalent ions from ICP-AES analyses regardless of their identical nominal dopant concentration (Table S4). The successful doping of Sn^{2+} in $CsPbBr_3$ QDs can be well established by the EDS element mapping of one single randomly selected $CsPbBr_3$:Sn^{2+} (4.3 mol %) QD, where Sn^{2+} ions are homogeneously distributed among the whole QD (Figure S14). More importantly, the PL intensity of excitonic luminescence for Sn^{2+}-doped $CsPbBr_3$ QDs was observed to be ~1.5 times stronger than that of their initial PL intensity after being heated to 200 °C and then cooled to room temperature (Figure S15). This experimental observation matches well our first-principles calculation showing that the absolute value of formation energy (−6.85 eV) for Sn^{2+}-doped $CsPbBr_3$ QDs was increased by 0.40 eV with respect to that of pure $CsPbBr_3$ QDs (Table S5). Likewise, enhanced excitonic luminescence was also detected in Cd^{2+}, Co^{2+}, Zn^{2+}, and Sr^{2+} ion-doped $CsPbBr_3$ QDs (Figure S16), accompanied by the simultaneously increased formation energies (Table S5). These results further confirm that the much improved thermal stability for $CsPbX_3$:Mn^{2+} QDs indeed originates from the enhanced formation energy.

The air stability for $CsPbX_3$ QDs doped with different Mn^{2+} contents was also investigated by coating them on the surface of a glass slide followed by exposure to ambient air conditions. Figure 5b shows the green PL brightness for pure and Mn-doped $CsPbBr_3$ QDs as a function of the exposure time. The green PL brightness for pure $CsPbBr_3$ QDs underwent a striking degradation to be nonluminous within 30 days under ambient air conditions. By contrast, a much slower degradation rate was observed for all $CsPbBr_3$:Mn QDs that retained their original PL brightness of ~60% within 120 days and then remained essentially unchanged with a further increase in the exposure time. Specifically, the green PL brightness for $CsPbBr_3$:Mn^{2+} QDs with a Mn^{2+} doping concentration higher than 5.6 mol % was instead observed to gradually increase with longer exposure time. Even for the most unstable perovskite $CsPbI_3$ QDs, their red PL brightness was observed to be maintained within 4−5 days, which is in stark contrast to the complete degradation of pure $CsPbI_3$ QDs within 2 days (Figure S17). Taken together, these results provide unequivocal evidence that the Mn^{2+} dopant plays a key role in enhancing the air stability of $CsPbX_3$ QDs, which is of great importance for optoelectronic engineering of long-term stable PLEDs.

DOI: 10.1021/jacs.7b04000
J. Am. Chem. Soc. 2017, 139, 11443−11450

As a proof-of-concept experiment, we then fabricated three types of green-emitting PLED devices by using pure $CsPbBr_3$ and $CsPbBr_3$:Mn (2.6 mol %) and $CsPbBr_3$:Mn (3.8 mol %) QDs as green light emitters (hereafter referred to as PLED-pure, PLED-Mn2.6, and PLED-Mn3.8, respectively). All the PLED devices adopt the same multilayer-structured architecture as previously reported,[25] which comprises indium tin oxide (ITO), poly(ethylenedioxythiophene):polystyrenesulfonate (PEDOT:PSS), poly-TPD, $CsPbBr_3$:Mn or pure $CsPbBr_3$ QDs, TPBi, LiF, and Al layers (Figure 6a). As compared in Figure 6b, all the PLED devices produce green electroluminescence (EL) centered at 512−515 nm with a narrow fwhm of ∼20 nm, which can be readily attributed to the band-edge emission of $CsPbBr_3$ QDs with only a ∼2 nm blue shift relative to their PL emission peak acquired from the corresponding QDs, indicating that the PLEDs based on the $CsPbBr_3$:Mn QDs have inherited the PL color purity of pure $CsPbBr_3$ QDs. Figure 6c and d show the current density/luminance−voltage characteristics for all the PLEDs. Although Mn^{2+} doping has no distinct impact on their current density−voltage features (Figure 6c), the PLED-Mn2.6 and PLED-Mn3.8 devices outperform the PLED-pure counterparts in terms of luminance, reaching their maximum luminance of 9971 and 9717 cd/m^2 under the applied voltages of 6.2 and 6.5 V, respectively (Figure 6d), with a ∼1.3-fold improvement relative to the PLED-pure counterpart (7493 cd/m^2 under the applied voltage of 6.6 V). More importantly, for the key performance parameters of the PLED device, the maximum EQE and CE were determined to increase from 0.81% and 3.71 cd/A for the PLED-pure device to 1.49% and 6.40 cd/A for the PLED-Mn3.8 device. Likewise, much more improved EQE and CE were also achieved in red-emitting PLEDs based on Mn^{2+}-doped $CsPbI_3$ QDs when compared to their pure counterparts (Figure S18 and Table S6). These values particularly for the maximum luminance for PLED-Mn2.6 and PLED-Mn3.8 devices are also comparable to those of most PLED devices previously reported (Table S6), which clearly manifest the significant advantages of Mn-doped $CsPbX_3$ QDSs against the undoped ones for the fabrication of high-performance optoelectronic devices. Furthermore, we would like to emphasize that all the measurements for the performance of these PLED devices were carried out under ambient air conditions without any encapsulation or protection, indicative of the good air stability of the PLED devices we fabricated. We believe that the EQE and CE for these PLED devices can be significantly improved via an overall optimization of current protocols including the quantum dot synthesis and purification, surface modification, and PLED device fabrication, which is currently under way.

■ CONCLUSIONS

In summary, we have proposed a simple but valid strategy through Mn^{2+} substitution to fundamentally stabilize the perovskite lattices of luminescent cesium lead halide perovskite QDs that suffer from poor thermal and air stability under ambient air conditions associated with their intrinsic low formation energies. Benefiting from the successful doping of Mn^{2+} ions in host lattices, the formation energies of perovskite $CsPbX_3$:Mn QDs were found to be enhanced when compared to their pure counterparts. As a result, high-quality perovskite $CsPbX_3$:Mn QDs with much better thermal and air stability and optical performance were obtained, which thus enables us to fabricate a series of high-performance PLEDs under ambient air conditions with higher EQE and CE relative to those devices using pure $CsPbX_3$ QDs as light emitters. The improved material stability along with higher device performance reveals that such a Mn^{2+}-substitution strategy might eventually open up a new avenue to eliminate the notorious limitation of poor thermal and environmental stability of $CsPbX_3$ QDs for the fabrication of efficient optoelectronic devices with excellent long-term stability.

■ EXPERIMENTAL DETAILS

Chemicals and Materials. All the chemical reagents were of analytical grade and were used as received without further purification. Cesium carbonate (Cs_2CO_3, 99.9%), lead(II) bromide ($PbBr_2$, ≥98%), lead(II) chloride ($PbCl_2$, 99.999%), lead(II) iodide (PbI_2, 99.999%), manganese(II) chloride tetrahydrate ($MnCl_2{\cdot}4H_2O$, 99.99%), manganese(II) bromide ($MnBr_2$, 98%), manganese(II) iodide (MnI_2, 98%), tin(II) bromide, oleic acid (OA, technical grade 90%), oleylamine (OAm, 80−90%), and 1-octadecene (ODE, 90%) were purchased from Sigma-Aldrich. Acetone, cyclohexane, *N*,*N*-dimethylformamide (DMF), and ethanol were purchased from Sinopharm Chemical Reagent Co., China.

Structural and Optical Characterization. XRD patterns of the samples were collected with an X-ray diffractometer (MiniFlex2, Rigaku) with Cu Kα1 radiation (λ = 0.154 187 nm). X-band EPR spectra for $CsPbX_3$ QDs dispersed in cyclohexane ($CsPbCl_3$) or DMF ($CsPbBr_3$ and $CsPbI_3$) were measured with an E 500 EPR spectrometer (Bruker-BioSpin) at room temperature with a 9.37 MHz microwave frequency and 20 mW microwave power. Both the TEM and high-resolution TEM measurements were performed by using a TECNAI G2F20 TEM. HAADF-STEM images for $CsPbX_3$:Mn QDs coupled with the EDS element mapping were obtained by utilizing a Titan G2 80-200 ChemiSTEM, FEI. PL emission, excitation spectra, and PL lifetimes were recorded on a spectrometer equipped with both continuous (450 W) xenon and pulsed flash lamps (FLS980, Edinburgh Instrument). For temperature-dependent PL measurements, the samples were put inside a Linkam THMS600E heating and freezing stage with a tunable temperature range from 77 to 873 K and heating rate of 60 °C min^{-1}. The QDs were in situ heated or cooled on the stage, whose temperature was controlled by a temperature controller (Linkam LNP95) to a certain temperature and held for 5 min to make the temperature stable, were measured for the PL spectra, and then proceeded to the next temperature point immediately. All the QDs were first heated from room temperature to high temperature (100, 150, and 200 °C) and then cooled to room temperature with a temperature interval of 10 °C. The absolute PL QYs for all samples were measured at room temperature by employing a barium sulfate coated integrating sphere (Edinburgh) as the sample chamber that was mounted on an FLS920 spectrometer with the entry and output port of the sphere located in 90° geometry from each other in the plane of the spectrometer. All the spectral data collected were corrected for the spectral response of both the spectrometer and the integrating sphere. PL photographs of the quantum dot solutions and solid samples were taken with a Nikon digital single lens reflex D100 upon UV excitation without using any filter. The EL spectra and density/luminance−voltage characteristics were collected by using a Keithley 2400 source, a fiber integration sphere, and a PMA-12 spectrometer for light output measurements in air and at room temperature.

General Procedure for the Synthesis of $CsPbX_3$:Mn (or Sn) QDs. $CsPbX_3$:Mn (or Sn) QDs were synthesized according to a modified colloidal synthetic approach previously reported.[2] In brief, a mixture of 0.188 mmol of PbX_2 and MnX_2 (or SnX_2) at a designated Mn/Pb mole ratio from 0 to 100 mol % was first added to a 50 mL two-neck flask containing 5 mL of ODE, 0.5 mL of OA, and 0.5 mL of OAm and degassed under a N_2 flow at room temperature for 20 min and then heated at 120 °C under a N_2 flow with constant stirring for 60 min to remove the moisture from the raw materials. Thereafter, the mixture was heated to 150 °C under a N_2 flow with constant stirring, followed by a rapid injection of 0.4 mL of the Cs-oleate precursor

DOI: 10.1021/jacs.7b04000
J. Am. Chem. Soc. 2017, 139, 11443−11450

mentioned above (0.125 M in ODE). After reacting for 5−10 s, the reaction mixture was cooled to 0 °C rapidly by using an ice−water bath to obtain monodisperse Mn^{2+}-doped $CsPbX_3$ QDs with an average nanocrystal size about 10 nm. The obtained QDs were collected by centrifugation at 12 000 rpm for 5 min and stored in a glovebox under argon protection.

General Procedure for the Fabrication of PLEDs. In brief, PEDOT:PSS solutions (Baytron PVPAl 4083, filtered through a 0.22 μm filter) were spin-coated onto the ITO-coated glass substrates at 3000 rpm for 60 s and baked at 140 °C for 15 min. Afterward, the hole transporting layer was prepared by spin-coating a poly-TPD chlorobenzene solution with a concentration of 6 mg mL^{-1} at 3000 rpm for 1 min, followed by the deposition of perovskite Mn^{2+}-doped $CsPbBr_3$ or pure $CsPbBr_3$ QDs dispersed in cyclohexane solution with a concentration of 15 mg/mL by spin coating at 3000 rpm for 60 s. Finally, TPBi (40 nm) and LiF/Al electrodes (1 nm/100 nm) were deposited using a thermal evaporation system through a shadow mask under a high vacuum of 2×10^{-4} Pa. The device active area was estimated to be 4 mm^2 as defined by the overlapping area of the ITO and Al electrodes.

First-Principle Calculations Based on DFT. The formation energies and bond lengths for $CsMnX_3$, $CsPbX_3$, and $CsPbX_3$:Mn(Sn) QDs were evaluated using the DFT plane-wave pseudopotential method as implemented in the CASTEP module integrated in the Material Studio 7.0 program package.[50] The Perdew−Burke−Ernzerhof[51] exchange and correlation functional with generalized gradient approximation and the ultrasoft pseudopotentials[52] were employed for all calculations. Taking both the computational assumption and accuracy into account, the kinetic energy cutoffs and Monkhorst−Pack *k*-point mesh size to sample the Brillouin zone were set variably for different systems. For the undoped systems, calculations including the structural optimization, properties, and energies were performed using a supercell containing 64 unit cells with a kinetic energy cutoff of 700 eV and *k*-points of 4 × 4 × 4. For Mn-doped $CsPbX_3$ systems, variable parameters were set with different doping contents of Mn^{2+} ions, which were classified as the following three cases: (a) for the low-doped systems with dopant content less than 4.0 mol %, the FINE quality energy cutoff and mesh size were employed; (b) for the medium-doped systems (a dopant content larger than 5.0% and less than 10.0 mol %), an energy cutoff of 400 eV and *k*-points of 4 × 4 × 4 were set; (c) for the high-doped systems (a dopant content larger than 10.0 mol %), the same calculation settings as the undoped systems were employed.

■ ASSOCIATED CONTENT

Supporting Information

The Supporting Information is available free of charge on the ACS Publications website at DOI: 10.1021/jacs.7b04000.

Additional experimental details, Figures S1−18, and Tables S1−6 (PDF)

■ AUTHOR INFORMATION

Corresponding Authors

*liuysh@fjirsm.ac.cn
*zeng.haibo@njust.edu.cn
*hmc@fjirsm.ac.cn
*xchen@fjirsm.ac.cn

ORCID

Haibo Zeng: 0000-0002-0281-3617
Xueyuan Chen: 0000-0003-0493-839X

Notes

The authors declare no competing financial interest.

■ ACKNOWLEDGMENTS

This work is supported by the Strategic Priority Research Program of the Chinese Academy of Sciences (XDB20000000 and XDA09030102), the 973 Program of MOST (No. 2014CB845605), the NSFC (Nos. 21390392, 21473205, U1305244, 51572128, 21325104, and 61604074), the CAS/SAFEA International Partnership Program for Creative Research Teams, Youth Innovation Promotion Association of CAS, and the Natural Science Foundation of Fujian Province (Nos. 2017I0018 and 2017J01038).

■ REFERENCES

(1) Akkerman, Q. A.; D'Innocenzo, V.; Accornero, S.; Scarpellini, A.; Petrozza, A.; Prato, M.; Manna, L. *J. Am. Chem. Soc.* **2015**, *137*, 10276.
(2) Protesescu, L.; Yakunin, S.; Bodnarchuk, M. I.; Krieg, F.; Caputo, R.; Hendon, C. H.; Yang, R. X.; Walsh, A.; Kovalenko, M. V. *Nano Lett.* **2015**, *15*, 3692.
(3) Zhang, D. D.; Eaton, S. W.; Yu, Y.; Dou, L. T.; Yang, P. D. *J. Am. Chem. Soc.* **2015**, *137*, 9230.
(4) Bekenstein, Y.; Koscher, B. A.; Eaton, S. W.; Yang, P. D.; Alivisatos, A. P. *J. Am. Chem. Soc.* **2015**, *137*, 16008.
(5) Hoffman, J. B.; Schleper, A. L.; Kamat, P. V. *J. Am. Chem. Soc.* **2016**, *138*, 8603.
(6) Lignos, I.; Stavrakis, S.; Nedelcu, G.; Protesescu, L.; Demello, A. J.; Kovalenko, M. V. *Nano Lett.* **2016**, *16*, 1869.
(7) Shamsi, J.; Dang, Z. Y.; Bianchini, P.; Canale, C.; Di Stasio, F.; Brescia, R.; Prato, M.; Manna, L. *J. Am. Chem. Soc.* **2016**, *138*, 7240.
(8) Wang, K. H.; Wu, L.; Li, L.; Yao, H. B.; Qian, H. S.; Yu, S. H. *Angew. Chem., Int. Ed.* **2016**, *55*, 8328.
(9) Song, J. Z.; Xu, L. M.; Li, J. H.; Xue, J.; Dong, Y. H.; Li, X. M.; Zeng, H. B. *Adv. Mater.* **2016**, *28*, 4861.
(10) Koscher, B. A.; Bronstein, N. D.; Olshansky, J. H.; Bekenstein, Y.; Alivisatos, A. P. *J. Am. Chem. Soc.* **2016**, *138*, 12065.
(11) Nedelcu, G.; Protesescu, L.; Yakunin, S.; Bodnarchuk, M. I.; Grotevent, M. J.; Kovalenko, M. V. *Nano Lett.* **2015**, *15*, 5635.
(12) Amgar, D.; Stern, A.; Rotem, D.; Porath, D.; Etgar, L. *Nano Lett.* **2017**, *17*, 1007.
(13) Protesescu, L.; Yakunin, S.; Bodnarchuk, M. I.; Bertolotti, F.; Masciocchi, N.; Guagliardi, A.; Kovalenko, M. V. *J. Am. Chem. Soc.* **2016**, *138*, 14202.
(14) Wang, Y.; Li, X. M.; Sreejith, S.; Cao, F.; Wang, Z.; Stuparu, M. C.; Zeng, H. B.; Sun, H. D. *Adv. Mater.* **2016**, *28*, 10637.
(15) Li, X. M.; Wu, Y.; Zhang, S. L.; Cai, B.; Gu, Y.; Song, J. Z.; Zeng, H. B. *Adv. Funct. Mater.* **2016**, *26*, 2435.
(16) Liu, Z.; Bekenstein, Y.; Ye, X.; Nguyen, S. C.; Swabeck, J.; Zhang, D.; Lee, S.-T.; Yang, P.; Ma, W.; Alivisatos, A. P. *J. Am. Chem. Soc.* **2017**, *139*, 5309.
(17) Song, J. Z.; Li, J. H.; Li, X. M.; Xu, L. M.; Dong, Y. H.; Zeng, H. B. *Adv. Mater.* **2015**, *27*, 7162.
(18) Dastidar, S.; Egger, D. A.; Tan, L. Z.; Cromer, S. B.; Dillon, A. D.; Liu, S.; Kronik, L.; Rappe, A. M.; Fafarman, A. T. *Nano Lett.* **2016**, *16*, 3563.
(19) Swarnkar, A.; Marshall, A. R.; Sanehira, E. M.; Chernomordik, B. D.; Moore, D. T.; Christians, J. A.; Chakrabarti, T.; Luther, J. M. *Science* **2016**, *354*, 92.
(20) Ling, Y.; Tian, Y.; Wang, X.; Wang, J. C.; Knox, J. M.; Perez-Orive, F.; Du, Y.; Tan, L.; Hanson, K.; Ma, B.; Gao, H. *Adv. Mater.* **2016**, *28*, 8983.
(21) Raino, G.; Nedelcu, G.; Protesescu, L.; Bodnarchuk, M. I.; Kovalenko, M. V.; Mahrt, R. F.; Stoferle, T. *ACS Nano* **2016**, *10*, 2485.
(22) Xu, Y. Q.; Chen, Q.; Zhang, C. F.; Wang, R.; Wu, H.; Zhang, X. Y.; Xing, G. C.; Yu, W. W.; Wang, X. Y.; Zhang, Y.; Xiao, M. *J. Am. Chem. Soc.* **2016**, *138*, 3761.
(23) Doane, T. L.; Ryan, K. L.; Pathade, L.; Cruz, K. J.; Zang, H. D.; Cotlet, M.; Maye, M. M. *ACS Nano* **2016**, *10*, 5864.
(24) Yakunin, S.; Protesescu, L.; Krieg, F.; Bodnarchuk, M. I.; Nedelcu, G.; Humer, M.; De Luca, G.; Fiebig, M.; Heiss, W.; Kovalenko, M. V. *Nat. Commun.* **2015**, *6*, 8056.
(25) Li, J. H.; Xu, L. M.; Wang, T.; Song, J. Z.; Chen, J. W.; Xue, J.; Dong, Y. H.; Cai, B.; Shan, Q. S.; Han, B. N.; Zeng, H. B. *Adv. Mater.* **2017**, *29*, 1603885.

DOI: 10.1021/jacs.7b04000
J. Am. Chem. Soc. 2017, 139, 11443−11450

(26) Zhou, H.; Yuan, S. P.; Wang, X. X.; Xu, T.; Wang, X.; Li, H. L.; Zheng, W. H.; Fang, P.; Li, Y. Y.; Sun, L. T.; Pan, A. L. *ACS Nano* **2017**, *11*, 1189.
(27) Amgar, D.; Aharon, S.; Etgar, L. *Adv. Funct. Mater.* **2016**, *26*, 8576.
(28) Zhang, X.; Lin, H.; Huang, H.; Reckmeier, C.; Zhang, Y.; Choy, W. C. H.; Rogach, A. L. *Nano Lett.* **2016**, *16*, 1415.
(29) Li, G.; Rivarola, F. W. R.; Davis, N. J. L. K.; Bai, S.; Jellicoe, T. C.; de la Peña, F.; Hou, S.; Ducati, C.; Gao, F.; Friend, R. H.; Greenham, N. C.; Tan, Z.-K. *Adv. Mater.* **2016**, *28*, 3528.
(30) Zhang, X.; Xu, B.; Zhang, J.; Gao, Y.; Zheng, Y.; Wang, K.; Sun, X. W. *Adv. Funct. Mater.* **2016**, *26*, 4595.
(31) Yantara, N.; Bhaumik, S.; Yan, F.; Sabba, D.; Dewi, H. A.; Mathews, N.; Boix, P. P.; Demir, H. V.; Mhaisalkar, S. *J. Phys. Chem. Lett.* **2015**, *6*, 4360.
(32) Palazon, F.; Akkerman, Q. A.; Prato, M.; Manna, L. *ACS Nano* **2016**, *10*, 1224.
(33) Wang, H. C.; Lin, S. Y.; Tang, A. C.; Singh, B. P.; Tong, H. C.; Chen, C. Y.; Lee, Y. C.; Tsai, T. L.; Liu, R. S. *Angew. Chem., Int. Ed.* **2016**, *55*, 7924.
(34) Sun, C.; Zhang, Y.; Ruan, C.; Yin, C. Y.; Wang, X. Y.; Wang, Y. D.; Yu, W. W. *Adv. Mater.* **2016**, *28*, 10088.
(35) Huang, S. Q.; Li, Z. C.; Kong, L.; Zhu, N. W.; Shan, A. D.; Li, L. *J. Am. Chem. Soc.* **2016**, *138*, 5749.
(36) Wang, Y. N.; He, J.; Chen, H.; Chen, J. S.; Zhu, R. D.; Ma, P.; Towers, A.; Lin, Y.; Gesquiere, A. J.; Wu, S. T.; Dong, Y. J. *Adv. Mater.* **2016**, *28*, 10710.
(37) Wang, F.; Han, Y.; Lim, C. S.; Lu, Y. H.; Wang, J.; Xu, J.; Chen, H. Y.; Zhang, C.; Hong, M. H.; Liu, X. G. *Nature* **2010**, *463*, 1061.
(38) Liu, W.; Lin, Q.; Li, H.; Wu, K.; Robel, I.; Pietryga, J. M.; Klimov, V. I. *J. Am. Chem. Soc.* **2016**, *138*, 14954.
(39) Dong, H.; Sun, L. D.; Wang, Y. F.; Ke, J.; Si, R.; Xiao, J. W.; Lyu, G. M.; Shi, S.; Yan, C. H. *J. Am. Chem. Soc.* **2015**, *137*, 6569.
(40) Feng, X. D.; Sayle, D. C.; Wang, Z. L.; Paras, M. S.; Santora, B.; Sutorik, A. C.; Sayle, T. X. T.; Yang, Y.; Ding, Y.; Wang, X. D.; Her, Y. S. *Science* **2006**, *312*, 1504.
(41) Begum, R.; Parida, M. R.; Abdelhady, A. L.; Murali, B.; Alyami, N. M.; Ahmed, G. H.; Hedhili, M. N.; Bakr, O. M.; Mohammed, O. F. *J. Am. Chem. Soc.* **2017**, *139*, 731.
(42) Parobek, D.; Roman, B. J.; Dong, Y.; Jin, H.; Lee, E.; Sheldon, M.; Son, D. H. *Nano Lett.* **2016**, *16*, 7376.
(43) Liu, H.; Wu, Z.; Shao, J.; Yao, D.; Gao, H.; Liu, Y.; Yu, W.; Zhang, H.; Yang, B. *ACS Nano* **2017**, *11*, 2239.
(44) Pradhan, N.; Peng, X. G. *J. Am. Chem. Soc.* **2007**, *129*, 3339.
(45) Guria, A. K.; Dutta, S. K.; Das Adhikari, S.; Pradhan, N. *ACS Energy Lett.* **2017**, *2*, 1014.
(46) Mir, W. J.; Jagadeeswararao, M.; Das, S.; Nag, A. *ACS Energy Lett.* **2017**, *2*, 537.
(47) Wu, B.; Zhou, Y. Y.; Xing, G. C.; Xu, Q.; Garces, H. F.; Solanki, A.; Goh, T. W.; Padture, N. P.; Sum, T. C. *Adv. Funct. Mater.* **2017**, *27*, 201604818.
(48) Xing, G. C.; Kumar, M. H.; Chong, W. K.; Liu, X. F.; Cai, Y.; Ding, H.; Asta, M.; Gratzel, M.; Mhaisalkar, S.; Mathews, N.; Sum, T. C. *Adv. Mater.* **2016**, *28*, 8191.
(49) Jellicoe, T. C.; Richter, J. M.; Glass, H. F. J.; Tabachnyk, M.; Brady, R.; Dutton, S. E.; Rao, A.; Friend, R. H.; Credgington, D.; Greenham, N. C.; Bohm, M. L. *J. Am. Chem. Soc.* **2016**, *138*, 2941.
(50) Clark, S. J.; Segall, M. D.; Pickard, C. J.; Hasnip, P. J.; Probert, M. J.; Refson, K.; Payne, M. C. *Z. Kristallogr. - Cryst. Mater.* **2005**, *220*, 567.
(51) Perdew, J. P.; Burke, K.; Ernzerhof, M. *Phys. Rev. Lett.* **1996**, *77*, 3865.
(52) Vanderbilt, D. *Phys. Rev. B: Condens. Matter Mater. Phys.* **1990**, *41*, 7892.

DOI: 10.1021/jacs.7b04000
J. Am. Chem. Soc. 2017, 139, 11443−11450